

Haldane phases and phase diagrams of the $S = \frac{3}{2}$ and $S = 1$ bilinear-biquadratic Heisenberg model on the orthogonal dimer chain

Ke Ren,¹ Muwei Wu,¹ Shou-Shu Gong^{1,2,3}, Dao-Xin Yao^{1,4,*} and Han-Qing Wu^{1,†}

¹Guangdong Provincial Key Laboratory of Magnetoelectric Physics and Devices, Center for Neutron Science and Technology,

School of Physics, Sun Yat-sen University, Guangzhou 510275, China

²School of Physical Sciences, Great Bay University, Dongguan 523000, China

³Great Bay Institute for Advanced Study, Dongguan 523000, China

⁴International Quantum Academy, Shenzhen 518048, China



(Received 28 July 2023; accepted 8 November 2023; published 1 December 2023)

We systematically study the effects of higher-order interactions on the $S = \frac{3}{2}$, 1 orthogonal dimer chains using exact diagonalization and density matrix renormalization group. Due to frustration and higher spin, there are rich quantum phases, including three Haldane phases, two gapless phases, and several magnetically ordered phases. To characterize these phases and their phase transitions, we study various physical quantities such as energy gap, energy-level crossing, fidelity susceptibility, spin correlation, entanglement spectrum, and central charge. According to our calculations, the biquadratic term can enhance the Haldane phase regions. In particular, we numerically identify that a Haldane phase in $S = \frac{3}{2}$ case is adiabatically connected to the exact AKLT (Affleck, Kennedy, Lieb, and Tasaki) point when adding a bicubic term. Our study on the orthogonal dimer model, which is a 1D version of the Shastry-Sutherland model, provides insights into understanding the possible $S = \frac{3}{2}$, 1 Haldane phases in quasi-1D and 2D frustrated magnetic materials.

DOI: [10.1103/PhysRevB.108.245104](https://doi.org/10.1103/PhysRevB.108.245104)

I. INTRODUCTION

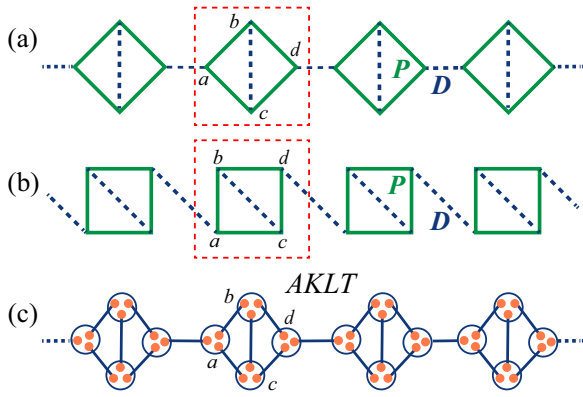
In 1983, Haldane classified the antiferromagnetic Heisenberg spin chains with integer and half-integer spin into two distinct classes [1,2]. For the integer case, the ground state which is called the Haldane phase has a finite excitation gap and short-range antiferromagnetic spin-spin correlations which decay exponentially with distance. Later, the exact gapped state with integer spins was clearly revealed by the so-called AKLT model proposed by Affleck, Kennedy, Lieb, and Tasaki with the biquadratic interaction on a spin-1 antiferromagnetic Heisenberg chain [3,4]. The ground state of the Haldane chain model can be adiabatically connected to the rigorous ground state of this AKLT model. For the AKLT state, each spin-1 can be seen as a combination of two symmetrized spin- $\frac{1}{2}$, and each spin- $\frac{1}{2}$ is connected by a singlet bond with another spin- $\frac{1}{2}$ on the nearest-neighbor sites. So, in general, under open boundary conditions (OBCs), there are two free spin- $\frac{1}{2}$ at the ends of the chain which form the edge states and induce the degeneracy of the ground state. Further research on topological properties reveals that the $S = 1$ Haldane phase on the 1D chain is a bosonic symmetry-protected topological phase, protected by time-reversal symmetry, D_2 symmetry, and inversion symmetry [5–8]. In experiments, the excitation energy gap and the edge state of the Haldane phase have been confirmed by some quasi-one-dimensional magnetic materials such as $\text{Ni}(\text{C}_2\text{H}_8\text{N}_2)_2\text{NO}_2(\text{ClO}_4)$ (NENP)

[9–11], Y_2BaNiO_5 [12–15], AgVP_2S_6 [16,17], and some other materials [18,19]. Some studies on organic materials found that triangulene can have high-spin ground states [20–24]. As the building block, triangulenes can be connected to form effective spin-1 chains with different lengths in which the finite excitation gap and the edge states have also been observed in experiments [22].

According to the proposal of Affleck *et al.*, more general exact AKLT states can be constructed if the spin magnitude S and the coordinate number z satisfy $z = 2S/n$, where n is an integer [3,4,25]. For $S = \frac{3}{2}$, we can construct an exact AKLT state using a bilinear-biquadratic-bicubic Heisenberg model on lattices with $z = 3$, such as an orthogonal dimer chain, hexagonal lattice, star lattice, and square-octagon lattice. For hexagonal lattice, Refs. [4,25] gave the exact ground state of the spin- $\frac{3}{2}$ AKLT model on this lattice and showed that the spin-spin correlations of this spin- $\frac{3}{2}$ AKLT state also decay exponentially. Based on these facts, the authors conjectured that the energy gap is also finite, although it is very difficult to give a strict proof [4,25]. Motivated by the potential application as a universal resource in measurement-based quantum computation [26–29], the hexagonal AKLT model has been further studied for many years [30–35] and most of the results support the existence of a finite gap [30,31,33–35]. Although the rigorous mathematical proof is still difficult to provide, Refs. [34,35] independently demonstrated that the spectral gap has a lower bound through a combination of mathematical analysis and numerical calculations. Different from the spin-1 Haldane phase on the 1D chain, the AKLT phase on a hexagonal lattice is a weak symmetry-protected topological phase protected by $\text{SO}(3)$ and translation symmetry [32,33].

*yaodaoy@mail.sysu.edu.cn

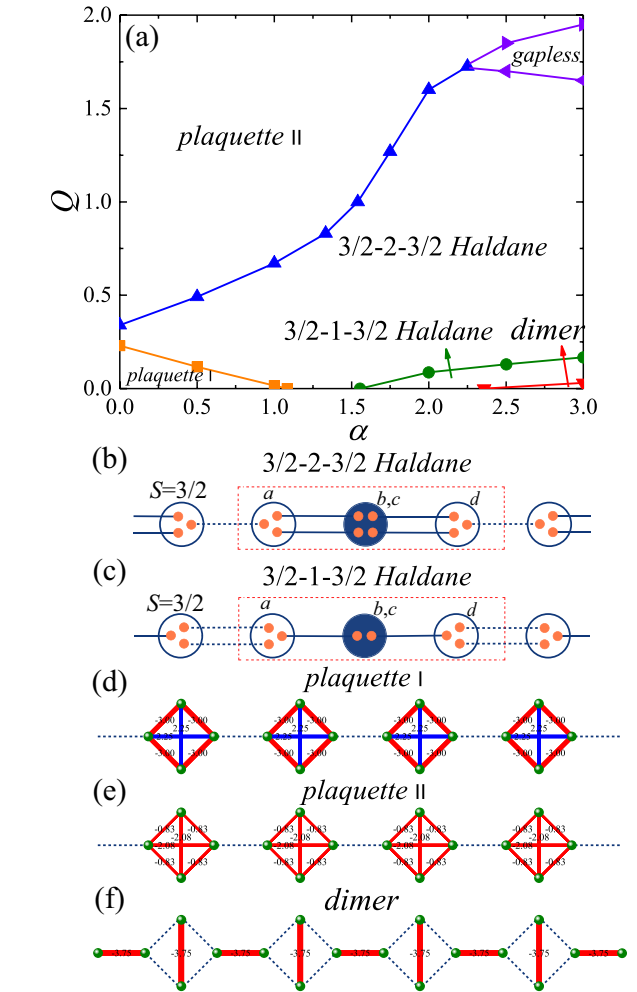
†wuhangq3@mail.sysu.edu.cn



Meanwhile, for the ladder, star lattice, square-octagon lattice, and other lattices with $z = 3$, there are also some studies on the spin- $\frac{3}{2}$ AKLT model [33,34,36].

Among these lattices with $z = 3$, the orthogonal dimer chain is a frustrated lattice which may have rich phases and can be well studied by the density-matrix renormalization group (DMRG) method due to its quasi-1D geometry. In addition, the orthogonal dimer chain is the 1D version of the 2D Shastry-Sutherland lattice [37–43], which can be used to describe the magnetic properties of $\text{SrCu}_2(\text{BO}_3)_2$ [44–49] and some other materials [50–53]. Therefore, exploring a possible frustration-induced Haldane phase in such a lattice with higher spins is a very interesting topic. By using nonlinear sigma model technique and exact diagonalization (ED), Koga and Kawakami found that there are $(2S + 1)$ spin-gap phases with different ratio of the intra- to the interdimer bilinear interaction on the spin- S orthogonal dimer chain, which are separated by first-order phase transitions [54]. They used valence bond solid pictures to show one and two Haldane phases for $S = 1$ and $S = \frac{3}{2}$ cases, respectively, which are also shown in Figs. 2(b), 2(c), and 10(a) in this paper. References [55,56] further showed the phase diagram with spin magnitude $S = 1$ after considering the effect of interchain bilinear interactions which connect the orthogonal dimer chain model to the 2D Shastry-Sutherland model. However, the lattice sizes of their numerical calculations are limited to a small size due to the exponential increasing of Hilbert space in ED calculation. Larger system sizes are needed to extrapolate to the thermodynamic limit using sophisticated numerical methods, such as DMRG. Moreover, higher order exchange interactions, such as biquadratic and bicubic interactions, are very sensitive for determining the magnetic ground state in frustrated higher spin systems. For the $S = \frac{3}{2}$ case, the exact relations between the Haldane phases with only a bilinear term and the exact

AKLT state with biquadratic and bicubic terms still need further studies.



AKLT state with biquadratic and bicubic terms still need further studies.

In this paper, we study the $S = \frac{3}{2}$, 1 Heisenberg model on quasi-one-dimensional orthogonal dimer chains with bilinear, biquadratic, and even bicubic interactions. We use ED and DMRG methods to determine the ground-state phase diagrams. From our calculations, we get rich phases and identify three Haldane phase regions characterized by several physical quantities, such as energy spectra and entanglement spectra.

After introducing the bicubic interaction for the spin- $\frac{3}{2}$ case, we identify that the $\frac{3}{2}$ -2- $\frac{3}{2}$ Haldane in Fig. 2(a) can be adiabatically connected to the rigorous AKLT point. We also identify several magnetic and other nonmagnetic phases, whose properties are characterized by studying on correlations, magnetic moments, and structure factors.

The rest of this paper is organized as follows. In Sec. II, we introduce the model Hamiltonian and some physical quantities used to determine the phase boundaries and characterize different phases. In Sec. III, we show the ground-state phase diagram and the quantum phase transitions of the $S = \frac{3}{2}$ bilinear-biquadratic model by calculating the energy spectra, entanglement spectra, quadrupolar correlation, and some other physical quantities. In addition, we further investigate the effect of bicubic interaction and study the connections between Haldane phases and the exact AKLT point. In Sec. IV, similar to the spin- $\frac{3}{2}$ case, we use ED and DMRG to study the phase diagram of the $S = 1$ bilinear-biquadratic model. Finally, a summary and discussion on our results is given in Sec. V.

II. MODEL AND METHOD

We study the $S = \frac{3}{2}$, 1 bilinear-biquadratic-bicubic model on the orthogonal dimer chain which is shown in Fig. 1(a). The Hamiltonian is defined as

$$H = \sum_{\langle i,j \rangle_P} [J\hat{S}_i \cdot \hat{S}_j + Q(\hat{S}_i \cdot \hat{S}_j)^2 + C(\hat{S}_i \cdot \hat{S}_j)^3] \\ + \alpha \sum_{\langle i,j \rangle_D} [J\hat{S}_i \cdot \hat{S}_j + Q(\hat{S}_i \cdot \hat{S}_j)^2 + C(\hat{S}_i \cdot \hat{S}_j)^3],$$

where \hat{S}_i is the spin- S ($S = \frac{3}{2}, 1$) operator at site i , P represents plaquette, while D represents dimer, $\langle i, j \rangle_P$ and $\langle i, j \rangle_D$ denote the sites on the bonds of plaquettes (P) and dimers (D), which are shown as green solid and blue dashed lines in Fig. 1(a), respectively. α controls the relative interaction strength on these two kinds of bonds. J , Q , and C are bilinear, biquadratic, and bicubic interactions, respectively. Similar to bilinear interaction J , the biquadratic and bicubic interactions can also be extracted from the Hubbard model, but with higher order perturbation expansion [57,58]. Meanwhile, the biquadratic interaction Q can also come from the spin-phonon coupling or lattice distortion effect [59,60]. In the following calculations, except for Secs. III B 4 and IV B 2, we set $J = 1$ as the energy unit.

In this paper, we use ED and DMRG to study the ground-state phase diagram of this model. By using ED, we obtain the low-energy spectra on the finite-size lattices up to 16 sites, in which the low-energy level crossings can be seen as signals of phase transitions. In the following ED calculations, if not mentioned, the energy spectrum is only calculated in the $M_z = 0$ sector, where M_z is the eigenvalue of total spin angular momentum along the z component. The finite-size ED result can also be used as guidance for the DMRG calculation on larger-size lattices. Here, we use two kinds of DMRG in our calculations. For the DMRG applied with spin rotational symmetry, by keeping up to 4000 SU(2) states, all numerical results are accurate enough and the truncation errors are smaller than 1×10^{-6} . For the DMRG using the ITENSOR

package [61], we mainly apply it to study the effect of bicubic interaction.

To identify the nature of different phases in the phase diagram, we calculate two kinds of structure factors. The first kind is the spin structure factor

$$S(\mathbf{q}) = \frac{1}{N} \sum_{i,j} \langle \hat{S}_i \cdot \hat{S}_j \rangle e^{i\mathbf{q} \cdot (\vec{r}_i - \vec{r}_j)},$$

and the second one is the quadrupolar structure factor

$$Q(\mathbf{q}) = \frac{1}{N} \sum_{i,j} \langle \hat{Q}_i \cdot \hat{Q}_j \rangle e^{i\mathbf{q} \cdot (\vec{r}_i - \vec{r}_j)},$$

where \hat{Q}_i is the quadrupolar operator and $\hat{Q}_i \cdot \hat{Q}_j = 2(\hat{S}_i \cdot \hat{S}_j)^2 + \hat{S}_i \cdot \hat{S}_j - 2\hat{S}_i^2 \hat{S}_j^2 / 3$ [62,63]. To do the Fourier transform of these structure factors, we use two-leg ladderlike geometry which is topologically equivalent to the original orthogonal dimer chain, as can be seen in Fig. 1(b).

To determine the phase boundaries of different phases in the phase diagram, we also calculate fidelity susceptibility

$$\chi_F(x) = \frac{2[1 - F(x)]}{N(\delta x)^2}, \quad F(x) = |\langle \Psi_0(x) | \Psi_0(x + \delta x) \rangle|.$$

The divergent tendency in fidelity susceptibility can also be seen as a signal of quantum phase transition.

In the characterization of Haldane phase, the degeneracy of ground-state energy induced by the edge states under OBCss is an important feature. Meanwhile, for topological quantum states, the low-lying entanglement spectrum of the bulk would correspond to the low-energy spectrum on the edge [64,65]. Therefore, we also use entanglement spectrum to characterize the Haldane phases.

We also study the entanglement entropy in gapless phase region and at the quantum critical lines. For the quasi-one-dimensional orthogonal dimer chain, in these gapless regions, the low-energy gapless excitation can be described by the conformal field theory (CFT) [66] and the entanglement entropy $S_l = -\text{Tr}[\hat{\rho}_l \ln \hat{\rho}_l]$ under periodic boundary conditions (PBCss) and OBCs will follow the Calabrese-Cardy formula [67]

$$S_l = \frac{c}{3} \ln \left[\frac{N_c}{\pi} \sin \left(\frac{\pi l}{N_c} \right) \right] + g, \text{ for PBCs,} \\ S_l = \frac{c}{6} \ln \left[\frac{N_c}{\pi} \sin \left(\frac{\pi l}{N_c} \right) \right] + g, \text{ for OBCs,}$$

where $N_c = N/4$ is the total number of unit cells in the system, l is the number of unit cells in the subsystem, $\hat{\rho}_l$ is the reduced density matrix of the subsystem, g is a model-dependent constant, and c is the central charge.

III. $S = \frac{3}{2}$ RESULTS

A. Bilinear model ($Q = 0, C = 0$)

First, we restudy the ground-state phase diagram of the $S = \frac{3}{2}$ bilinear model ($Q = 0, C = 0$) on the orthogonal dimer chain. According to Ref. [54], using ED with small lattice sizes, there are four distinct gapped phases, including plaquette I, $\frac{3}{2}$ -2- $\frac{3}{2}$ Haldane, 3/2-1-3/2 Haldane and dimer phases with tuning α , and the phase transitions between these

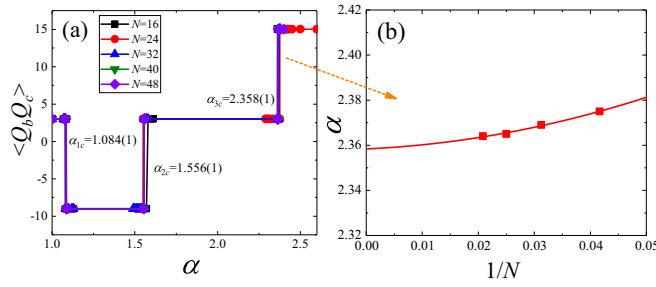


FIG. 3. (a) The quadrupolar correlations $\langle \hat{Q}_b \cdot \hat{Q}_c \rangle$ at $Q = 0$ in spin $S = \frac{3}{2}$ orthogonal dimer chain as functions of α . (b) The second-order polynomial fitting shows that the phase transition between $\frac{3}{2}$ - $1-\frac{3}{2}$ Haldane and dimer phases indicated by the orange arrow is located at $\alpha = 2.358(1)$ in the thermodynamic limit.

phases are all the first-order ones. Due to the commutation relationship $[(\hat{S}_b + \hat{S}_c)^2, \hat{H}] = 0$, $(\hat{S}_b + \hat{S}_c)^2$ shares the same eigenvectors with the Hamiltonian. And $(\hat{S}_b + \hat{S}_c)^2 |\psi\rangle = S_{\text{eff}}(S_{\text{eff}} + 1) |\psi\rangle$, where S_{eff} is equal to 2 and 1 in the two Haldane phases, respectively. Therefore, we label these two Haldane phases as $\frac{3}{2}$ - $2-\frac{3}{2}$ and $\frac{3}{2}$ - $1-\frac{3}{2}$ Haldane phases, where the middle index represents the effective spin-2 or -1 formed by two physical spins at the b and c sublattices, as shown in Figs. 2(b) and 2(c). When α is large, the system is in a dimer phase whose ground state can be adiabatically connected to the direct product of orthogonal dimers, and each dimer shares the same wave function $|\Psi_0\rangle = \frac{1}{2} |-\frac{3}{2}, \frac{3}{2}\rangle - \frac{1}{2} |-\frac{1}{2}, \frac{1}{2}\rangle + \frac{1}{2} |\frac{1}{2}, -\frac{1}{2}\rangle - \frac{1}{2} |\frac{3}{2}, -\frac{3}{2}\rangle$, which can be seen in Fig. 2(f). Similarly, when α is small, the plaquette-I phase can be adiabatically connected to the direct product of the four-site singlet state on isolated plaquettes, which will be further discussed in Sec. III B 1.

By using DMRG, we recalculate the phase boundaries with larger-size lattices. Due to the discontinuity of the first-order transition, we use the abrupt change of quadrupolar correlation to detect the phase transition points. As shown in Fig. 3(a), there are three discontinuities in the quadrupolar correlation $\langle \hat{Q}_b \cdot \hat{Q}_c \rangle$ between site b and site c in the first unit cell with the increase of α . For the phase transition between $\frac{3}{2}$ - $1-\frac{3}{2}$ Haldane and dimer phases, α_c gradually decreases with the increase of N (the number of sites in the lattice), which can be seen in Fig. 3(b). The second-order polynomial fitting of α_c shows that the phase transition point is located at $\alpha_c = 2.358(1)$ in the thermodynamic limit. For the other two phase transitions, the corresponding α_c obtained on lattices with $N = 40$ and 48 are almost the same. So, we can take the transition points $\alpha_c = 1.084(1)$ and $1.556(1)$ obtained on the largest lattice size $N = 48$, which is shown in Fig. 3(a).

B. Bilinear-biquadratic model ($Q \neq 0, C = 0$)

1. plaquette I, plaquette II, $\frac{3}{2}$ - $2-\frac{3}{2}$ Haldane

As shown in Fig. 2(a), there are other phases after adding biquadratic interaction, in which the origin of plaquette I, plaquette II, and $\frac{3}{2}$ - $2-\frac{3}{2}$ Haldane can be discussed from an isolated plaquette limit with $\alpha = 0$.

The energy spectrum of one plaquette with four lattice sites is shown in Fig. 14(a) of Appendix A. When Q is zero,

four $S = \frac{3}{2}$ spins form a unique singlet state with a finite excitation gap. When $Q \gtrsim 0.34$, there is another four-site singlet state with a unique ground state and an excitation gap. These two states are different singlet states with different real-space spin correlations, as can be seen in Figs. 2(d) and 2(e) [also shown in Figs. 14(b) and 14(c)]. Between these two singlet states, there is another state with multiple ground-state degeneracy.

When $\alpha > 0$, due to the finite gap protection, as shown in Fig. 2(a), the ground states in small Q and large Q are adiabatically connected to the direct product of corresponding four-site singlet states in isolated plaquette limit. We name these two different plaquette phases as plaquette I and plaquette II, respectively. As shown in Fig. 15 of Appendix A, the real-space spin correlations of these two plaquette phases agree well with the illustrations in Figs. 2(d) and 2(e). Both for plaquette I and plaquette II, the spin correlations between different plaquettes are relatively weak. The main difference between these two plaquette phases is the spin correlation in each plaquette. Especially, the spin correlations between diagonal sites in each plaquette are positive for plaquette I but negative for plaquette II.

For the case $Q \sim 0.3$, there is massive degeneracy when many plaquettes are decoupled, after adding a finite α , these degenerate states will lift, and the system goes into a Haldane phase due to the order-by-disorder mechanism. According to our calculations, this phase is adiabatically connected to the $\frac{3}{2}$ - $2-\frac{3}{2}$ Haldane phase at $Q = 0$ without any gap closing.

The Haldane-type phase can be identified by looking at the degeneracy of the energy spectrum under OBCs and entanglement spectrum under PBCs. Therefore, to further characterize the intermediate $\frac{3}{2}$ - $2-\frac{3}{2}$ Haldane phase and its quantum phase transition, we show the energy spectrum and entanglement spectrum along $\alpha = 1.0, Q > 0$ vertical line, shown in Figs. 4(a)–4(c). For the energy spectrum under OBCs and entanglement spectrum under PBCs, there is a region in the middle where the lowest spectrum levels with quantum number $S = 0$ and $S = 1$ are (quasi)degenerate. Instead, for the energy spectrum under PBCs, the triplet gap $\Delta_T = E_0(S = 1) - E_0(S = 0)$ as the lowest energy gap is finite in the corresponding region and has a maximum at $Q \sim 0.4$, which is shown in Fig. 4(a). These are consistent with the valence bond solid picture of $\frac{3}{2}$ - $2-\frac{3}{2}$ Haldane shown in Fig. 2(b). Under PBCs, all virtual $S = \frac{1}{2}$ spins form a singlet in pairs and the excitation from this ground state needs to break the singlets which lead to a finite gap in the energy spectrum. But in the open chain, the first spin at the a sublattice or the last spin at the d sublattice has only one neighboring effective $S = 2$ spin, which can be viewed as four virtual $S = \frac{1}{2}$ particles. These four virtual $S = \frac{1}{2}$ particles form two pairs of singlets at each side, leaving one virtual $S = \frac{1}{2}$ particle at each edge unpaired, as can be seen in Fig. 2(b). Two unpaired virtual $S = \frac{1}{2}$ particles from two edge sites contribute to the twofold degeneracy (with total spin angular momentum $S = 0$ and 1) at $M_z = 0$ subspace of ground-state energy under OBCs and entanglement spectrum under PBCs, as shown in Figs. 4(b) and 4(c). Here we mention that the commutation relationship $[(\hat{S}_b + \hat{S}_c)^2, \hat{H}] = 0$ is no longer established when $Q \neq 0$. But the above analysis still holds and

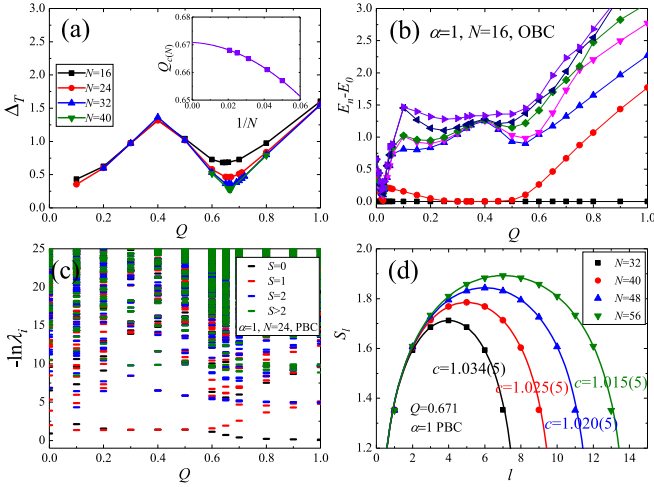


FIG. 4. (a) The finite-size triplet gap $\Delta_T = E_0(S=1) - E_0(S=0)$ of $S = \frac{3}{2}$ bilinear-biquadratic model along $\alpha = 1.0$ vertical line in the α - Q plane [see Fig. 2(a)] under periodic boundary condition. The inset is the second-order polynomial extrapolation of the phase transition point Q_c . (b) The energy spectrum under open boundary condition (OBCs) as a function of Q . The lattice sites used here is $N = 16$. (c) The entanglement spectrum with $N = 24$ under PBCs. (d) The entanglement entropy at $\alpha = 1.0, Q = 0.671$ where is at the phase transition point between $\frac{3}{2}$ - 2 - $\frac{3}{2}$ Haldane and plaquette II. The results obtained on different sizes of lattices and the corresponding central charges c are displayed with different colors.

the $\frac{3}{2}$ - 2 - $\frac{3}{2}$ Haldane phase extends to a more broad α region after adding biquadratic interaction.

Next, we study the quantum phase transitions among $\frac{3}{2}$ - 2 - $\frac{3}{2}$ Haldane, plaquette I, and plaquette II along $\alpha = 1$ vertical line in the α - Q plane. The phase transition from plaquette I to $\frac{3}{2}$ - 2 - $\frac{3}{2}$ Haldane is a first-order one at around $Q_c = 0.016(1)$, which can be verified by the singlet gap closing and reopening, which causes the discontinuity of correlation functions. More details about how we get the phase transition points can be found in Appendix B. For the quantum phase transition between $\frac{3}{2}$ - 2 - $\frac{3}{2}$ Haldane and plaquette II, the triplet gap $\Delta_T = E_0(S=1) - E_0(S=0)$ will close in the thermodynamic limit. As shown in Fig. 4(a), we identify the corresponding Q_c with numerically finding the position of minimum triplet gap on different sizes of lattices, and then using second-order polynomial extrapolation to get the quantum critical point $Q_c \approx 0.671$ in thermodynamic limit. Moreover, Fig. 4(d) shows the entanglement entropy S_l at this critical point under PBCs, and the fitted central charge $c \approx 1$, which indicates that this critical point may belong to the Wess-Zumino-Witten (WZW) $SU(2)_{k=1}$ CFT [68–70].

2. Gapless phase

As shown in Fig. 2(a), with increasing α , the phase transition line between $\frac{3}{2}$ - 2 - $\frac{3}{2}$ Haldane and plaquette II turns into a gapless phase region. And this is mainly identified based on the study of lowest triplet gaps [$\Delta_T = E_0(S=1) - E_0(S=0)$].

In the upper corner region of Fig. 2(a) ($\alpha \geq 2.0, Q \geq 1.5$), the triplet gaps as the lowest energy gaps change little

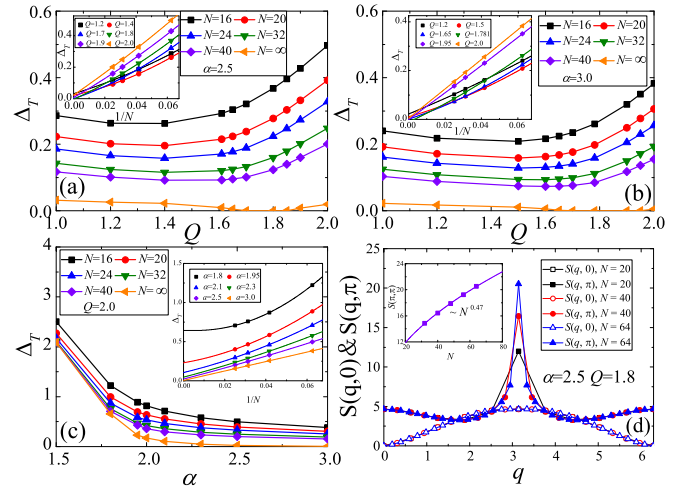


FIG. 5. (a), (b) The triplet gap Δ_T obtained with different system sizes under PBCs, and the parameter path is taken along $\alpha = 2.5$ and $\alpha = 3.0$ vertical line in the α - Q plane, respectively. The gapless region gradually expands with increasing α . (c) The triplet gap Δ_T along $Q = 2.0$ horizontal line in the α - Q plane. The insets of (a)–(c) show the extrapolation of the triplet gap Δ_T with the lattice sizes. (d) The spin structure factors $S(\mathbf{q})$ at $\alpha = 2.5, Q = 1.8$ along q_x from 0 to 2π in the Brillouin zone (BZ). The hollow symbols denote the results at $q_y = 0$ and solid symbols denote the results at $q_y = \pi$. The scaling behavior of spin structure factors $S(\pi, \pi)$ with system size N are shown in the inset of (d).

with different biquadratic interaction Q . To determine phase boundaries of this gapless region, we calculate the triplet gaps Δ_T at different parameters under PBCs and extrapolate the gaps with the inverse system sizes, which are shown in Figs. 5(a)–5(c) and their insets. When the extrapolated gaps are zero or negative, we believe that the triplet gaps $\Delta_T = 0$ in the thermodynamic limit. Along the $\alpha = 2.5$ vertical path in the α - Q plane, the triplet gaps Δ_T vanish when $1.7 \lesssim Q \lesssim 1.85$, while along $\alpha = 3.0$ vertical path, the gapless region is $1.65 \lesssim Q \lesssim 1.95$. Therefore, there is a finite gapless phase region at the upper right corner of the α - Q plane [see Fig. 2(a)] and the region of this phase gradually expands with growing α , as shown in Fig. 2(a).

To further characterize this gapless phase, we also study the structure factor at $\alpha = 2.5, Q = 1.8$. As shown in Fig. 5(d), the spin structure factors $S(\mathbf{q})$ obtained on different sizes of lattices have a singularity at (π, π) . As shown in the inset of Fig. 5(d), the spin structure factor $S(\pi, \pi)$ at this parameter increases as a function N^δ ($\delta \sim 0.47$), while the quadrupolar structure factors show no singularity. That indicates the existence of quasi-long-range spin correlation in this gapless phase, similar to the Luttinger liquid phase in the $S = \frac{1}{2}$ isotropic Heisenberg chain.

3. $\frac{3}{2}$ - 1 - $\frac{3}{2}$ Haldane

As shown in Fig. 2(a), the $\frac{3}{2}$ - 1 - $\frac{3}{2}$ Haldane phase region is smaller compared to $\frac{3}{2}$ - 2 - $\frac{3}{2}$ Haldane phase. In this phase, when $Q = 0$, the effective spin formed by two physical spins at b and c sublattices is $S_{\text{eff}} = 1$. Therefore, as shown in Fig. 2(c), only one $S = \frac{1}{2}$ virtual spin at each end site (a or d sublattice)

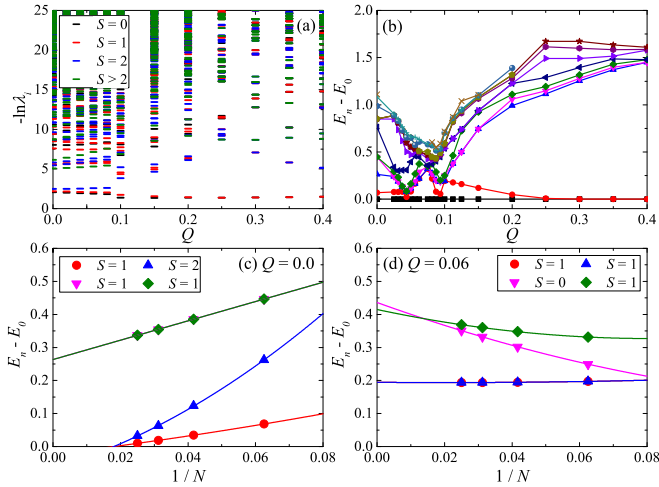


FIG. 6. (a) The entanglement spectrum as a function of Q along $\alpha = 2.0$ obtained with $N = 32$ under PBCs. (b) The energy spectrum along $\alpha = 2.0$ obtained with $N = 16$ under OBCs. (c), (d) The extrapolation of several lowest excitation gaps under OBCs at $\alpha = 2.0$, $Q = 0.0$ and 0.06 , respectively.

participates in the singlet pair, leaving four unpaired $S = 1/2$ virtual spins under OBCs. At $\alpha = 2.0$ and $Q = 0$, from the extrapolation of excitation gaps under OBCs shown in Fig. 6(c), the ground state has threefold degeneracy (total spin $S = 0, 1, 2$) at $M_z = 0$ subspace which correspond to combinations of the four unpaired virtual $S = 1/2$ spins (with two at each site). For the entanglement spectrum under PBCs, as shown in Fig. 6(a), three lowest spectrum levels under the subspace of $M_z = 0$ are separated by a gap with higher spectra and the total spins of these three spectrum levels are also $S = 0, 1$, and 2 , respectively. With the increase of Q , as shown in Figs. 6(b) and 6(d), it is interesting to see that the energy spectrum under OBCs has a nondegenerate region for $Q \sim 0.06$. But the lowest three entanglement spectrum levels under PBCs still seem to be degenerate, as shown in Fig. 6(a), and no phase transition signals can be seen in the energy spectrum under PBCs around this point, no matter what the system size is in our calculation. Therefore, we believe that it is still the $\frac{3}{2}$ - 1 - $\frac{3}{2}$ Haldane phase in this region.

The quantum phase transitions between $\frac{3}{2}$ - 1 - $\frac{3}{2}$ Haldane and dimer, $\frac{3}{2}$ - 2 - $\frac{3}{2}$ Haldane are all the first order with direct ground-state level crossings of singlet states. More details about these phase transitions can be seen in Appendix B. With further growing Q , as shown in Figs. 6(a) and 6(b), it enters the $\frac{3}{2}$ - 2 - $\frac{3}{2}$ Haldane phase whose lowest spectrum level has twofold degeneracy (total spin $S = 0$ and 1) at $M_z = 0$ subspace both for the entanglement spectrum under PBCs and energy spectrum under OBCs.

4. $J = \cos\theta$, $Q = \sin\theta$ ($\alpha = 1.0$)

Considering that the bilinear interaction J and biquadratic interaction Q may be either antiferromagnetic or ferromagnetic (FM) in the real materials [22,71,72], it is significant to map out the full phase diagram under the competition between bilinear and biquadratic interactions. Here, following the study of the bilinear-biquadratic $S = 1$ spin chain [73–75],

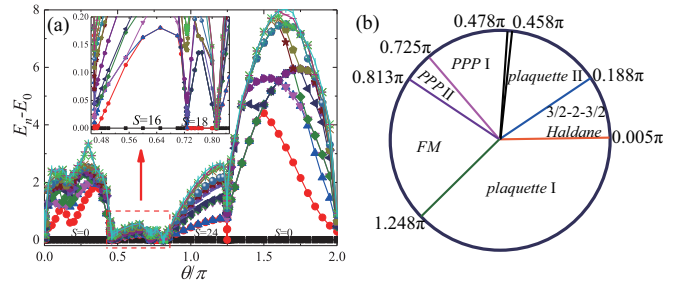


FIG. 7. (a) The low-energy spectrum as a function of θ/π which is obtained by ED on 16-site lattice under PBCs. The inset shows an enlarged drawing of the region labeled by a red dashed box in (a). (b) The ground-state phase diagram of spin- $\frac{3}{2}$ orthogonal dimer chain with $J = \cos\theta$, $Q = \sin\theta$, and $\alpha = 1.0$.

we set $J = \cos\theta$, $Q = \sin\theta$ to study the full phase diagram, while keeping $\alpha = 1.0$, $C = 0$.

When $0 \leq \theta < 0.353\pi$ ($Q/J = 2.0$), the phase transition points between plaquette I, $\frac{3}{2}$ - 2 - $\frac{3}{2}$ Haldane, and plaquette II are already shown in Fig. 2(a). Here, by converting Q_c to θ_c , we can easily obtain these two critical points in the phase diagram shown in Fig. 7(b). For these three phases, the ground states are all singlet states ($S = 0$) while for the FM phase at around $\theta = \pi$, the total spin of ground state is $S = 3N/2$, where N is the number of sites in the lattice.

From the energy spectrum shown in Fig. 7(a), in between plaquette II and FM, there are some regions (labeled by a red dashed box) where the excitation gaps are relatively small. After zooming in on these regions, we find three different phase regions where the total spins of ground states are, respectively, $S = 15, 16$, and 18 on the 16-site lattice under PBCs. To identify the nature of these three phase regions, we add a small pinning field ($-HS_1^z, H/J = 10^{-6}$) on the first site on the left which breaks the lattice translational symmetry and $U(1)$ symmetry, and then calculate the average magnetic moment $m = \frac{1}{N} \sum_i S_i^z$. As shown in Fig. 8(a), in between plaquette II ($m = 0$) and FM ($m = 3/2$), the curves of magnetic moment per site have another two plateaus ($m = 1$ and $9/8$) on the eight-site lattice and an extra small plateau with $m = 15/16$ on the 16-site lattice, which is consistent with the low-energy spectrum shown in Fig. 7(a). Figures 8(c) and 8(d) show the expectation value of magnetic moment $\langle S_i^z \rangle$ at each lattice site after adding the pinning field. Both at $\theta = 2\pi/3$ and 0.77π , $\langle S_i^z \rangle$ are always positive and less than $3/2$ (fully polarized case). Therefore, we name the phases with $m = 1$ and $9/8$ as partial polarized phase I (PPP I) and partial polarized phase II (PPP II), respectively. In addition, between plaquette II and PPP I, there is an extremely small parameter region which corresponds to the $m = 15/16$ magnetic plateau on the 16-site lattice and it is difficult to identify its phase boundaries in the thermodynamic limit using DMRG. Here, we use a 32-site lattice to get the phase transition points.

Next, we want to determine the phase transition points between PPP I, PPP II, FM, and plaquette I. Through DMRG calculations on larger-size lattices, we find that with increasing lattice size, the total spins of the ground states are $S = N, 9N/8, 3N/2, 0$ in PPP I, PPP II, FM and plaquette I, respectively. Especially, for FM, $|3/2, 3/2, \dots, 3/2, 3/2\rangle$,

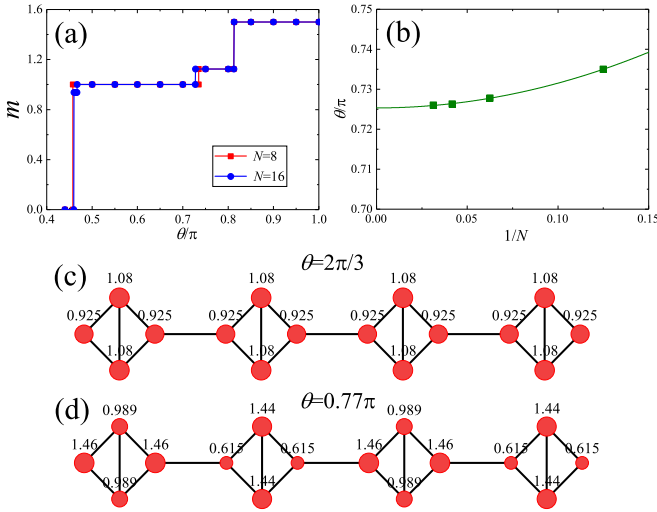


FIG. 8. (a) The average magnetic moment curve at different θ under a small pinning field ($= 10^{-6}$) on the first site from left. The results are obtained by ED on lattices with $N = 8$ and 16 under PBCs. (b) The second-order polynomial extrapolation of the phase transition point θ_c between PPP I and PPP II. (c) and (d), respectively, show the expectation value of magnetic moment (S_i^z) at each lattice site with $\theta = 2\pi/3$ and 0.77π .

$| -3/2, -3/2, \dots, -3/2, -3/2 \rangle$ are two degenerate ground states and the corresponding ground-state energy is $E_{FM} = \frac{27N}{8} \cos(\theta) + \frac{243N}{32} \sin(\theta)$. So, we can take crossings between the two lowest energies of $E_0(S = N)$, $E_0(S = 9N/8)$, E_{FM} , and $E_0(S = 0)$ as the signals of phase transitions among these four phases. As shown in Fig. 8(b), by the second-order polynomial fitting, we identify that the phase transition point between PPP I and PPP II is $\theta_c = 0.725\pi$. For the transition points between PPP II, FM, and plaquette I, which are nearly independent on system sizes, we can get two accurate phase transition points $\theta_c = 0.813\pi$ and $\theta_c = 1.248\pi$ using 16-site lattice. In the phase diagram shown in Fig. 7(b), except for the continuous quantum phase transition between the $\frac{3}{2}$ - 2 - $\frac{3}{2}$ Haldane phase and plaquette II phase, other phase transitions are all first order.

C. Exact AKLT point ($\alpha = 1.0$)

For the spin- $\frac{3}{2}$ orthogonal dimer chain whose coordinate number $z = 3$, the exact AKLT point is located at $\alpha = 1.0$, $Q = 116/243$, $C = 16/243$ [4]. As shown in Fig. 1(c), at the exact solvable AKLT point, each spin- $\frac{3}{2}$ on a site can be seen as a combination of three virtual $S = \frac{1}{2}$ particles which, respectively, form a singlet with one of three neighbor sites. Under PBCs, as shown in the inset of Fig. 9(a), the lowest triplet gap $\Delta_T = E_0(S = 1) - E_0(S = 0)$ as the first-excited gap changes little with increasing system size. The second-order polynomial extrapolation shows that the lowest excitation gap of this AKLT state under PBCs is $\Delta_T \sim 1.412$ in the thermodynamic limit, which is much larger than the lower bound of the spin- $\frac{3}{2}$ AKLT state on a hexagonal lattice and some other lattices with coordinate number $z = 3$ [34,35]. While under OBCs, as shown in the inset of Fig. 9(a), two unpaired virtual $S = \frac{1}{2}$ particles at the edge lead to the

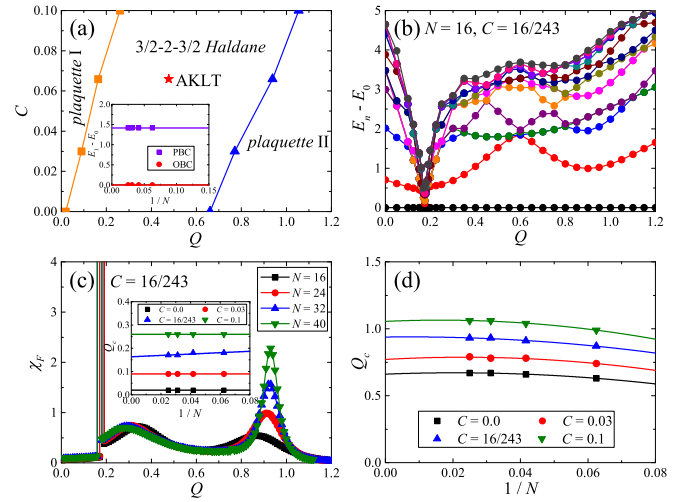


FIG. 9. (a) The ground-state phase diagram in the Q - C plane with $\alpha = 1.0$, and the red star represents the exact AKLT point. The inset shows the extrapolation of the first excitation gap at exact AKLT point under PBCs and OBCs. (b) The low-energy spectrum along $C = 16/243$ obtained by ED with $N = 16$ under PBCs. (c) The fidelity susceptibility for different system sizes along $C = 16/243$. The inset is the linear extrapolation of the phase transition points between plaquette I and $\frac{3}{2}$ - 2 - $\frac{3}{2}$ Haldane at different C . (d) The second-order polynomial extrapolation of the phase transition points between $\frac{3}{2}$ - 2 - $\frac{3}{2}$ Haldane and plaquette II at different C .

twofold degenerate ground state at $M_z = 0$ subspace, and this is quite similar to the $\frac{3}{2}$ - 2 - $\frac{3}{2}$ Haldane phase. Both of them share the same edge state. Therefore, it would be interesting to investigate the connection between $\frac{3}{2}$ - 2 - $\frac{3}{2}$ Haldane and the AKLT point as well as the effect of bicubic interaction C .

As shown in Fig. 9, we study the phase diagram with bilinear, biquadratic, and bicubic interactions while keeping $\alpha = 1.0$. Figure 9(b) shows the low-energy spectrum varying with Q while keeping $C = 16/243$, and this result is obtained on the 16-site lattice under PBCs. It can be seen that the singlet gap rapidly decreases at $Q \approx 0.175$, and this is a strong signal of the first-order phase transition. With growing Q , the triplet gap has a minimum at $Q \approx 0.9$ which may also indicate the existence of a phase transition. At the same time, as shown in Fig. 9(c), there are three peaks in the fidelity susceptibility. The second peak would not diverge in the thermodynamic limit, and only the first and third peaks can be seen as the signals of phase transitions. By extrapolations shown in the inset of Figs. 9(c) and 9(d), we obtain the phase transition points using different C . It should be noted that at $C = 0$, the phase transition points determined by the fidelity susceptibility are consistent with that obtained by quadrupolar correlation and energy spectra in Fig. 2(a) ($C = 0$). As shown in Fig. 9(a), no new phases are induced by C and the phase diagram is still divided into three phase regions: plaquette I, $\frac{3}{2}$ - 2 - $\frac{3}{2}$ Haldane, and plaquette II with increasing Q . We find that the AKLT point is located in the $\frac{3}{2}$ - 2 - $\frac{3}{2}$ Haldane phase region and the exact AKLT state is in the same phase as the $\frac{3}{2}$ - 2 - $\frac{3}{2}$ Haldane phase at $C = 0$.

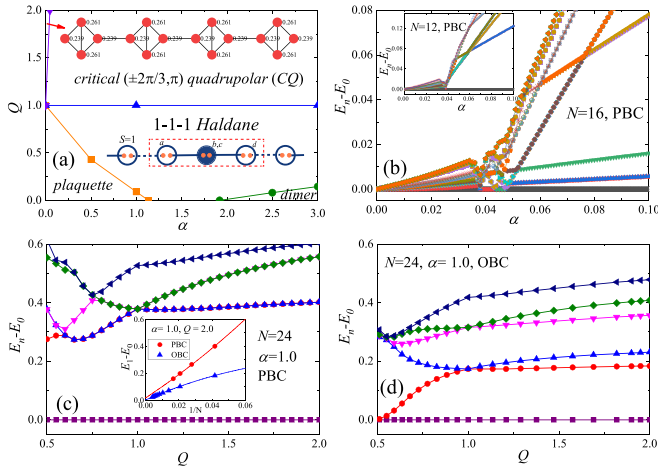


FIG. 10. (a) The ground-state phase diagram of spin-1 orthogonal dimer chain with bilinear-biquadratic interaction. The valence bond solid picture of 1-1-1 Haldane is shown in (a). The expectation value of magnetic moment $\langle S_i^z \rangle$ on each lattice site in the partial polarized phase at $\alpha = 0.03$, $Q = 2.0$ is also shown in the position where the red arrow points. (b) The energy spectrum along $Q = 2.0$ with $\alpha \leq 0.1$, which is obtained by ED on 16-site lattice under PBCs. The result obtained on 12-site lattice under PBCs is also shown in the inset of (b). (c), (d) The energy spectrum along $\alpha = 1.0$ obtained on lattices with $N = 24$ under PBCs and OBCs, respectively. The inset in (c) shows the extrapolation of the first-excitation gaps at $\alpha = 1.0$, $Q = 2.0$ under PBCs and OBCs.

IV. $S = 1$ RESULTS

In this section, we study the ground-state phase diagram of the $S = 1$ bilinear-biquadratic model on the orthogonal dimer chain.

A. Bilinear model ($Q = 0$)

Similar to the spin- $\frac{3}{2}$ case, we start from a restudy of the bilinear model ($Q = 0$). The phase diagram includes three distinct gapped phases: plaquette, 1-1-1 Haldane, and dimer, with the increase of α , and the phase transitions are all first order. For the 1-1-1 Haldane phase, as shown in the inset of Fig. 10(a), the physical spins of b and c sublattices form an effective spin-1, resulting in a similar valence bond solid picture and edge state as the Haldane phase of spin-1 chain. The dimer phase can be adiabatically connected to the direct product of the two-site singlet state $|\Psi_0\rangle = \frac{1}{\sqrt{3}}| -1, 1 \rangle - \frac{1}{\sqrt{3}}|0, 0\rangle + \frac{1}{\sqrt{3}}|1, -1\rangle$. The plaquette phase can be adiabatically connected to the direct product of the four-site singlet state in an isolated plaquette limit with $\alpha = 0$, which will be further discussed in Sec. IV B 1.

By using DMRG with up to 48 sites under PBCs, we recalculate the phase transition points between these three phases. As shown in Fig. 18(a) of Appendix B, the quadrupolar correlation $\langle \hat{\mathbf{Q}}_b \cdot \hat{\mathbf{Q}}_c \rangle$ shows two abrupt changes which indicate the first-order phase transitions. The phase transition points are located at $\alpha_{c1} = 1.135(5)$ and $\alpha_{c2} = 1.815(5)$, which are shown in the horizontal axis of Fig. 10(a) and in Fig. 18(a) of Appendix B.

B. Bilinear-biquadratic model ($Q \neq 0$)

1. α - Q phase diagram

After considering the biquadratic interaction Q , as shown in Fig. 10(a), besides plaquette, 1-1-1 Haldane, and dimer phases, there are also a partial polarized phase and a critical gapless phase with dominant quadrupolar correlation at $\vec{k} = (\pm 2\pi/3, \pi)$. In the phase diagram, the phase transition from 1-1-1 Haldane to the critical gapless phase is a Berezinskii-Kosterlitz-Thouless (BKT) phase transition, while from 1-1-1 Haldane to plaquette and dimer, the phase transitions are both the first-order which are determined by the discontinues in $\langle \hat{\mathbf{Q}}_b \cdot \hat{\mathbf{Q}}_c \rangle$ shown in Fig. 18 of Appendix B.

As shown in Fig. 16(a) of Appendix A, in the low-energy spectra of a plaquette, there is an energy-level closing at $Q = 1.0$ which separates a plaquette singlet state and a four-site quintuplet state ($S = 2$). The effect of adding a small α to these two states differs greatly. When $Q < 1.0$, protected by the finite gap, the ground state can be adiabatically connected to the direct product of four-site singlets, which is a plaquette phase. When $Q > 1.0$, the quintuplet state of a plaquette has fivefold degeneracy distributed in $M_z = 0, \pm 1$, and ± 2 subspace. Many decoupled plaquettes at $\alpha = 0$ will contribute to the highly degenerate ground state. After adding α , the system goes into a very narrow region of magnetic phase shown in Fig. 10(a). As shown in Fig. 10(b), there are many low-energy spectrum levels with quite small excitation gaps in this phase. Due to the absence of $k = (\pm 2\pi/3, \pi)$ in the Brillouin zone of the lattice with $N = 16$, this lattice size cannot correctly catch the critical $k = (\pm 2\pi/3, \pi)$ quadrupolar phase at larger α , which leads to some fictitious level closings near $\alpha \sim 0.04$ in Fig. 10(b). To show the detail of the magnetic order, we also add a small pinning field ($= 10^{-6}$) on the first site at $\alpha = 0.03$, $Q = 2.0$ and calculate the expectation value of magnetic moment $\langle S_i^z \rangle$ on each lattice site, which is shown in the inset of Fig. 10(a) and indicates a partial polarized phase.

As shown in Fig. 10(a), at larger Q , there is another phase above 1-1-1 Haldane. To identify this phase, we calculate the real-space spin correlation and find that $\langle \hat{\mathbf{S}}_b \cdot \hat{\mathbf{S}}_c \rangle$ keeps at -1 in this phase and 1-1-1 Haldane along $\alpha = 1$ vertical line in the α - Q plane, which indicates that the two physical spins at b and c sublattices form an effective spin-1. So in these two phase regions, the orthogonal dimer chain can be effectively seen as a spin-1 trimer chain and the low-energy spectrum as well as the phase diagram would be close to the uniform spin-1 chain. For $S = 1$ spin chain, at $Q/J = 1$, there is a BKT phase transition between Haldane phase and a gapless phase with dominant $k = \pm 2\pi/3$ quasi-long-range quadrupolar correlations [74–76]. Similarly, the phase at larger Q in an orthogonal dimer chain may also be a gapless phase with quadrupolar correlations.

To confirm this conjecture, we calculate the spin and quadrupolar structure factors on lattices up to 60 sites under PBCs, and show the results of $\alpha = 1.0$, $Q = 2.0$ in Figs. 11(a) and 11(b). Both the spin and quadrupolar structure factors have singularities at $(\pm 2\pi/3, \pi)$. As shown in Fig. 11(c), with increasing $\ln N$, $Q(2\pi/3, \pi)$ at $Q = 2.0$ is larger and increases faster than that at $Q = 1.0$, while the situation for $S(2\pi/3, \pi)$ reverses. So, at $Q = 2.0$, it has dominant

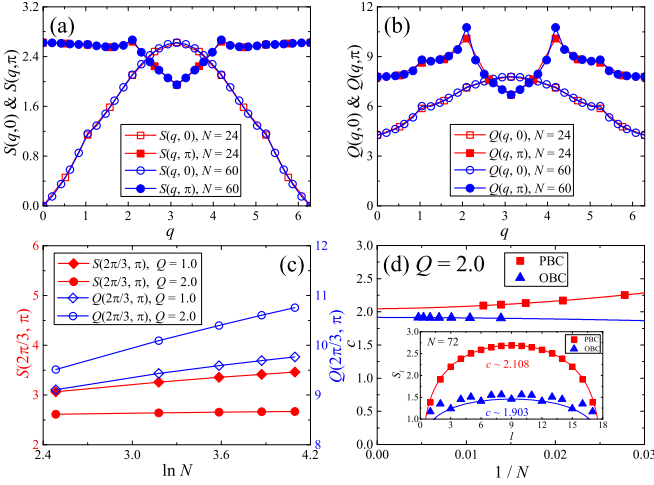


FIG. 11. (a) The spin structure factors $S(q)$ and (b) quadrupolar structure factors $Q(q)$ at $\alpha = 1.0$, $Q = 2.0$. In (a) and (b), the hollow symbols denote the results at $q_y = 0$ and solid symbols denote the results at $q_y = \pi$. (c) The spin structure factor $S(2\pi/3, \pi)$ and quadrupolar structure factor $Q(2\pi/3, \pi)$ at different Q vary with $\ln N$. The blue hollow symbols and the red solid symbols represent $Q(2\pi/3, \pi)$ and $S(2\pi/3, \pi)$, respectively. The diamond symbols and cycle symbols represent the results obtained at $\alpha = 1.0$, $Q = 1.0$ and $Q = 2.0$, respectively. (d) Extrapolation of the central charge obtained at $\alpha = 1.0$, $Q = 2.0$ under PBCs and OBCs. The inset shows the entanglement entropy S_l obtained on 72-site lattice. The central charge under OBCs are obtained by fitting S_l where l is multiple of three due to the $\vec{k} = (\pm 2\pi/3, \pi)$ quadrupolar correlations.

$\vec{k} = (\pm 2\pi/3, \pi)$ quadrupolar correlations. In the meanwhile, we show the low-energy spectra of this phase in Figs. 10(c) and 10(d). Here, we choose the lattice size to be the multiple of 12 to contain $(\pm 2\pi/3, \pi)$ in the Brillouin zone. Under both PBCs and OBCs, the total spin of the first-excited state is $S = 2$ and the energy gap is extrapolated to almost zero in the thermodynamic limit, as can be seen in the inset of Fig. 10(c). Based on these results, we identify that the phase above the 1-1-1 Haldane in Fig. 10(a) is a critical phase with dominant quadrupolar correlation at $\vec{k} = (\pm 2\pi/3, \pi)$. We also show the central charge of this gapless phase in Fig. 11(d). After breaking the translation symmetry under OBCs, as shown in the inset of Fig. 11(d), the entanglement entropy S_l shows a period of 3 due to the $\vec{k} = (\pm 2\pi/3, \pi)$ quadrupolar correlations in this phase. So, the central charges under OBCs are obtained by fitting the entropy S_l where l is multiple of three. The number of data used in the fitting would be less than that obtained under PBCs with the same lattice size, which may induce stronger finite-size effect on the central charge fitted under OBCs. As shown in Fig. 11(d), the central charges at $\alpha = 1.0$, $Q = 2.0$ are extrapolated to $c \approx 2$ both under PBCs and OBCs, which is also similar with the critical quadrupolar phase on spin-1 chain [74,75].

Next, we want to find the phase transition point between this critical quadrupolar phase and 1-1-1 Haldane. A direct idea is that it may also be a BKT phase transition and located at $Q = 1.0$, like the $S = 1$ spin chain. We first calculate the fidelity susceptibility under PBCs and extrapolate the corresponding Q_c of the peaks with the lattice size. The

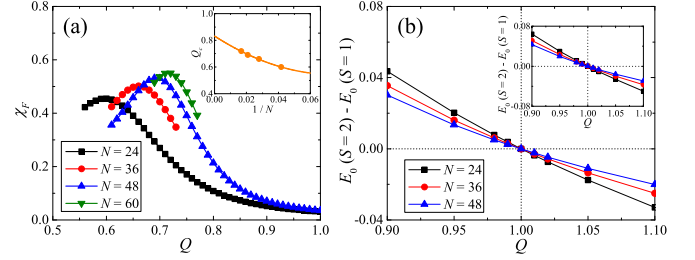


FIG. 12. (a) Fidelity susceptibility varies with Q along $\alpha = 1.0$ obtained by DMRG on different lattice sizes. The inset of (a) shows the second-order polynomial extrapolation of Q_c . (b) The energy gap $E_0(S = 2) - E_0(S = 1)$ between the lowest quintuplet state ($S = 2$) and the lowest triplet state ($S = 1$) varies with Q along $\alpha = 1.0$, and the energy gap $E_0(S = 2) - E_0(S = 1)$ along $\alpha = 3.0$ is also shown in the inset of (b).

extrapolated Q_c is smaller than 1 as shown in the inset of Fig. 12(a). However, fidelity susceptibility is difficult to obtain the exact BKT phase transition point in the J_1 - J_2 chain and some other models [77]. The same problem may also be encountered in the orthogonal dimer chain. In contrast, using energy-level crossing to determine the phase transition point can have a smaller finite-size effect and obtain more accurate results [43,78–80]. As shown in Figs. 10(c) and 10(d), the lowest triplet state ($S = 1$) and the lowest quintuplet state ($S = 2$) crosses at $Q = 1.0$. Similar crossings can also be seen in the low-energy spectra of the spin-1 chain at the phase transition point ($Q/J = 1$) between the Haldane phase and the critical quadrupolar phase [74–76]. By calculating the lowest energy in the sectors with total spin $S = 1$ and 2 under PBCs, we show $E_0(S = 2) - E_0(S = 1)$ varies little with Q along $\alpha = 1.0$ line in Fig. 12(b). The lowest triplet state always crosses with the lowest quintuplet state at $Q = 1.0$ with different lattice sizes. That indicates that the phase transition point should be $Q = 1.0$, $\alpha = 1.0$. As shown in the inset of Fig. 12(b), for $\alpha = 3.0$, the energy-level crossing also occurs at $Q = 1.0$ with different lattice sizes. Therefore, we believe that the phase boundary of 1-1-1 Haldane and the critical quadrupolar phase is a horizontal line at $Q = 1.0$ as shown in Fig. 10(a).

2. $J = \cos\theta$, $Q = \sin\theta$ ($\alpha = 1.0$)

To show the full competition between bilinear and bi-quadratic interactions, we also set $J = \cos\theta$, $Q = \sin\theta$ to study the full phase diagram along $\alpha = 1.0$. Except for plaquette, 1-1-1 Haldane, and the critical quadrupolar phase, there is another FM phase sandwiched by the critical quadrupolar phase and plaquette. The phase boundaries of this FM phase are exactly the same for all system sizes. From the energy spectrum shown in Fig. 13(a), we identify the phase transition points between these three phases are located at $\theta_c = 0.5\pi$ and 1.25π . And the full phase diagram is shown in Fig. 13(b).

V. SUMMARY AND DISCUSSION

By using ED and DMRG methods, we study the phase diagram of $S = \frac{3}{2}$, 1 bilinear-biquadratic Heisenberg model on

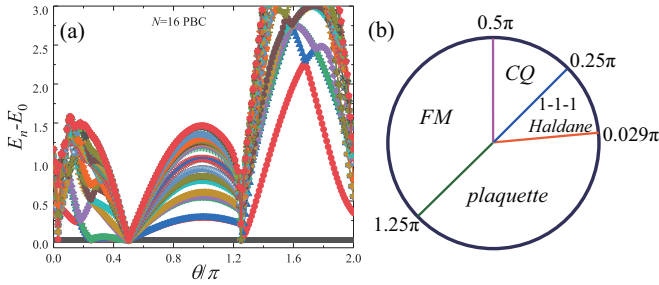


FIG. 13. (a) The low-energy spectrum as a function of θ/π which is obtained by ED on 16-site lattice under PBCs. (b) The ground-state phase diagram of spin-1 orthogonal dimer chain with $J = \cos\theta$, $Q = \sin\theta$, and $\alpha = 1.0$.

the orthogonal dimer chain. For the spin- $\frac{3}{2}$ case, we identify two Haldane phases, $\frac{3}{2}$ - 2 - $\frac{3}{2}$ Haldane and $\frac{3}{2}$ - 1 - $\frac{3}{2}$ Haldane. The region of the $\frac{3}{2}$ - 2 - $\frac{3}{2}$ Haldane can be expanded to a larger region by the biquadratic interaction Q . After considering the bicubic interaction, this $\frac{3}{2}$ - 2 - $\frac{3}{2}$ Haldane can be adiabatically connected to the exact AKLT point on spin- $\frac{3}{2}$ orthogonal dimer chain. Apart from the Haldane phases, there are also two plaquette phases, a dimer phase and a gapless phase in the phase diagram. We identify the nature of these phases from different aspects and determine the phase boundary between different phases. Most of the phase transitions are first order, except that between $\frac{3}{2}$ - 2 - $\frac{3}{2}$ Haldane and plaquette II, which is continuous with central charge $c \approx 1$. At $\alpha = 1.0$, we also set $J = \cos\theta$, $Q = \sin\theta$ and obtain the phase diagram for $\theta \in [0, 2\pi]$, in which we find another two partial polarized phases and a small undefined region which is needed for further study in the future. In addition, we also study the spin-1 case and identify a 1-1-1 Haldane in the phase diagram, whose edge state is the same as the Haldane phase in the spin-1 chain. With larger Q , there is a gapless critical phase with dominant quadrupolar correlation at $\vec{k} = (\pm 2\pi/3, \pi)$ in the phase diagram.

If adding the interchain interaction, the quasi-1D orthogonal dimer chain can form the 2D Shastry-Sutherland lattice. In experiments, it may be possible to synthesize such a Shastry-Sutherland lattice with weakly coupled orthogonal dimer chain and higher spins. The main physics can be dominated by this quasi-1D chain and it would be interesting to confirm our numerical results in experiments. Another possible way to construct the orthogonal dimer chain with higher effective spin is to use the organic triangulene which has been successfully used to construct the effective spin-1 Haldane chain materials [22]. In theory, for the first case, it would be interesting to investigate the evolution of the ground-state phase diagram from 1D to 2D, and identify the possible 2D Haldane phases in the Shastry-Sutherland model. As an analogy, for the spin-1 Haldane chain, without biquadratic interaction, it would quickly enter a Néel phase with only a small interchain interaction [81–86]. But after adding biquadratic interaction, an infinite projected entangled pair states study suggested that the Haldane phase can extend to the 2D square limit with increasing interchain interaction [86]. However, a DMRG study on spin-1 square lattice did not find this Haldane phase and, instead, they found a nematic spin liquid phase near the $SU(3)$ symmetry point, which cannot be adiabatically connected to

the 1D Haldane phase based on their calculation of spin correlation with different interchain interactions and biquadratic interactions [87]. This nematic spin liquid phase on spin-1 square lattice has also been studied by Refs. [88–90]. For the orthogonal dimer chain, by using ED on a 16-site lattice, Refs. [55,56] studied the effect of interchain interaction on the spin-1 bilinear model and claimed that 1-1-1 Haldane can exist to the 2D limit with increasing interchain interaction. However, due to the limited size, it is still worthy to study using more sophisticated numerical methods. Also, the effect of biquadratic interaction may enhance the Haldane phase region and make it easier to appear in the 2D case. Furthermore, recent theoretical [41,42] and experimental [46,49] studies suggest that $\text{SrCu}_2(\text{BO}_3)_2$ and the corresponding model on the Shastry-Sutherland lattice are good platforms for the investigation of the deconfined quantum critical point (DQCP). As a good starting point, our work on the quasi-1D orthogonal dimer chain will be helpful for further research on finding the DQCP in 2D frustrated system with $S > 1/2$.

ACKNOWLEDGMENTS

This work was supported by NKRDPC2022YFA1402802, NKRDPC-2018YFA0306001, NSFC-11804401, NSFC-11974432, NSFC-92165204, NSFC-11832019, NSFC-11874078, NSFC-11834014, Guangdong Provincial Key Laboratory of Magnetoelectric Physics and Devices (2022B1212010008), Leading Talent Program of Guangdong Special Projects (201626003), Shenzhen International Quantum Academy (SIQA202102), and Guangzhou Basic and Applied Basic Research Foundation (202201011569). We also acknowledge the support from the Dongguan Key Laboratory of Artificial Intelligence Design for Advanced Materials.

APPENDIX A: DECOUPLED LIMIT

As shown in Fig. 1(a), when the interactions between the sites on the bonds of dimers (blue dashed lines) are zero ($\alpha = 0$), the orthogonal dimer chain is decoupled into some isolated plaquettes. By studying the bilinear-biquadratic Heisenberg model ($C = 0$) on one plaquette, we can obtain the ground-state properties when α is zero or small.

In the spin- $\frac{3}{2}$ case, as shown in Fig. 14(a), the ground states of four-site plaquettes are both singlet states when $Q \lesssim 0.23$ and when $Q \gtrsim 0.34$. But the spin correlations are quite different at $Q = 0.0$ and 1.0 , especially for the spin correlations between diagonal sites, which can be seen in Figs. 2(d) and 2(e) [also shown in Figs. 14(b) and 14(c)]. This indicates that the ground states in the small Q and large Q regions are two kinds of singlet states. As shown in Fig. 15, after introducing a small α to connect the isolated plaquettes, protected by the finite excitation gap, the spin correlations between different plaquettes are still relatively weak, and the spin correlations in each plaquette are quite similar to that in the decoupled limit, which are also consistent with that shown in Figs. 2(d) and 2(e). Therefore, these two phases can be adiabatically connected to the direct product of two different singlet states at $\alpha = 0$, which are named as plaquette I and plaquette II.

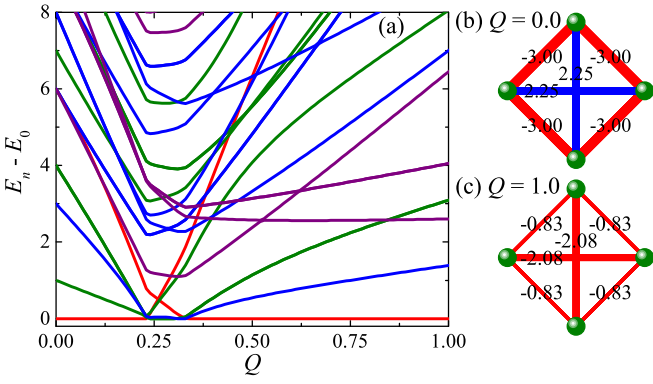


FIG. 14. (a) The energy spectra of a $S = \frac{3}{2}$ plaquette, in which the excited gaps with different total spin $S = 0, 1, 2$, and $S > 2$ are represented by red, green, blue, and purple lines, respectively. The real-space spin correlations between different sites in a plaquette at $\alpha = 0, Q = 0$, and $\alpha = 0, Q = 1.0$ are, respectively, shown in (b) and (c), which have also been shown in Figs. 2(d) and 2(e).

In the spin-1 case, as shown in Fig. 16(a), there is a level crossing at $Q = 1.0$. When $Q < 1.0$, the ground state is a singlet state ($S = 0$). In Fig. 16(b), we show the spin correlations at $Q = 0$. When $\alpha > 0$, similar to the spin- $\frac{3}{2}$ case, the ground state can also be adiabatically connected to the direct product of the four-site singlets, which is named the plaquette phase. For $Q > 1.0$, the ground state of the plaquette is a fivefold degenerate quintuplet state ($S = 2$) distributed in $M_z = 0, \pm 1$, and ± 2 subspaces. Therefore, the ground state is highly degenerate with many decoupled plaquettes at $\alpha = 0$. When α is not zero, there is a quite narrow magnetic phase and then it quickly enters the critical ($\pm 2\pi/3, \pi$) quadrupolar phase at a very small Q , which is shown in Figs. 10(a) and 10(b).

APPENDIX B: FIRST-ORDER PHASE TRANSITION POINTS

As shown in Figs. 2 and 10(a), there are many first-order phase transitions both in spin- $\frac{3}{2}$ and spin-1 case. At these transition points, the quadrupolar correlations $\langle \hat{Q}_b \cdot \hat{Q}_c \rangle$ show abrupt changes, which can be seen in Figs. 3, 17, and 18. By using DMRG to obtain the corresponding critical points α_c or Q_c on different sizes of lattices, we can finally determine these first-order phase transition points.

In the spin- $\frac{3}{2}$ case, when the biquadratic interaction $Q = 0$, we have shown the quadrupolar correlations $\langle \hat{Q}_b \cdot \hat{Q}_c \rangle$ in Fig. 3 and discussed the determination of three first-order phase transition points among plaquette I, $\frac{3}{2}$ - 2 - $\frac{3}{2}$ Haldane,

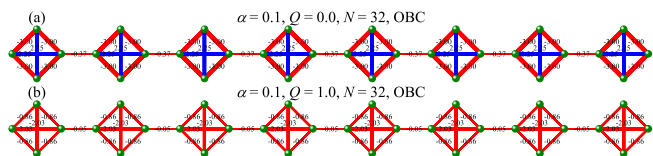


FIG. 15. The real-space spin correlation on $S = \frac{3}{2}$ orthogonal dimer chain with $N = 32$ under OBCs.

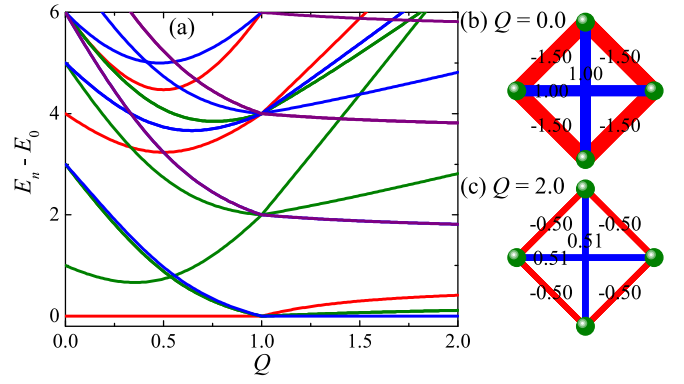


FIG. 16. (a) The energy spectra of a $S = 1$ plaquette, in which the excited gaps with different total spins $S = 0, 1, 2$, and $S > 2$ are represented by red, green, blue, and purple lines, respectively. The real-space spin correlations between different sites in a plaquette at $\alpha = 0, Q = 0$, and $\alpha = 0, Q = 2.0$ are shown in (b) and (c), respectively.

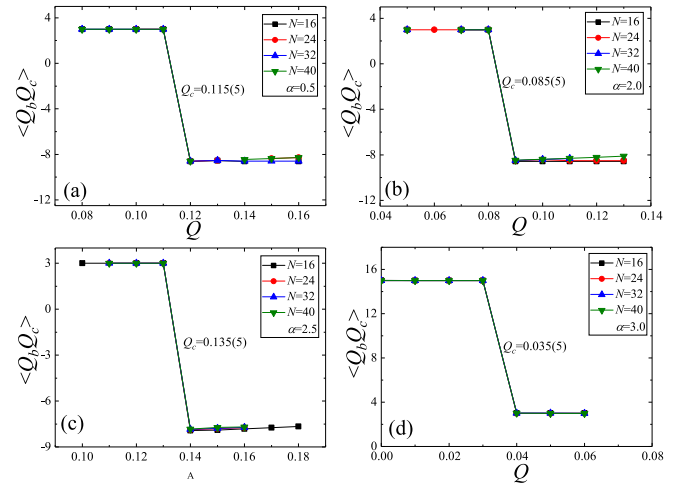


FIG. 17. (a)–(d) The quadrupolar correlations $\langle \hat{Q}_b \cdot \hat{Q}_c \rangle$ at $\alpha = 0.5, 2.0, 2.5$, and 3.0 , respectively.

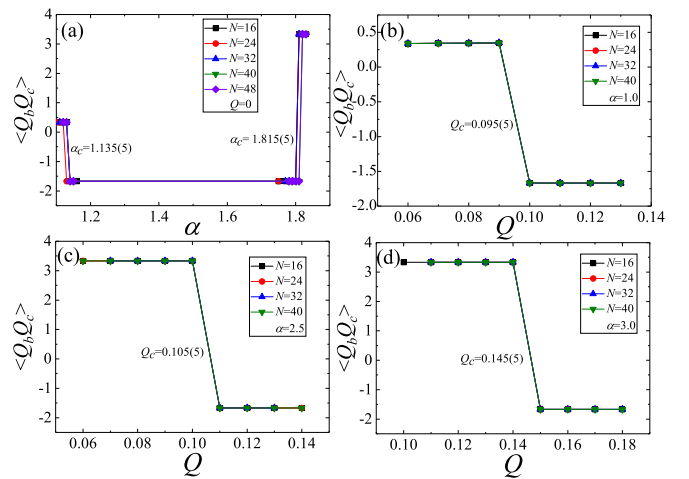


FIG. 18. (a) The quadrupolar correlations $\langle \hat{Q}_b \cdot \hat{Q}_c \rangle$ at $Q = 0$ in spin $S = 1$ orthogonal dimer chain as functions of α . (b)–(d) The quadrupolar correlations $\langle \hat{Q}_b \cdot \hat{Q}_c \rangle$ at $\alpha = 1.0, 2.5$ and 3.0 , respectively.

$\frac{3}{2}$ -1- $\frac{3}{2}$ Haldane, and dimer phases in the main text. Here, we show more results after considering biquadratic interaction Q in Figs. 17(a)–17(d). It can be seen that the transition points are almost independent on the lattice sizes, so they are determined by results of the largest lattice sizes used in the calculation. The corresponding values of the phase transition points are shown in Fig. 17.

In the spin-1 case, as shown in Fig. 18, the situations are quite similar. The critical points obtained on large-size lattices are always almost the same. Therefore, we use the results obtained on lattices with $N = 48$ (when $Q = 0$) and $N = 40$ (when $Q > 0$) to determine the first-order phase transition points between different phases whose values are also shown in Fig. 18.

-
- [1] F. Haldane, Continuum dynamics of the 1-D Heisenberg antiferromagnet: Identification with the O(3) nonlinear sigma model, *Phys. Lett. A* **93**, 464 (1983).
- [2] F. D. M. Haldane, Nonlinear field theory of large-spin Heisenberg antiferromagnets: Semiclassically quantized solitons of the one-dimensional easy-axis Néel state, *Phys. Rev. Lett.* **50**, 1153 (1983).
- [3] I. Affleck, T. Kennedy, E. H. Lieb, and H. Tasaki, Rigorous results on valence-bond ground states in antiferromagnets, *Phys. Rev. Lett.* **59**, 799 (1987).
- [4] I. Affleck, T. Kennedy, E. H. Lieb, and H. Tasaki, Valence bond ground states in isotropic quantum antiferromagnets, *Commun. Math. Phys.* **115**, 477 (1988).
- [5] X. Chen, Z.-C. Gu, Z.-X. Liu, and X.-G. Wen, Symmetry protected topological orders and the group cohomology of their symmetry group, *Phys. Rev. B* **87**, 155114 (2013).
- [6] Z.-C. Gu and X.-G. Wen, Tensor-entanglement-filtering renormalization approach and symmetry-protected topological order, *Phys. Rev. B* **80**, 155131 (2009).
- [7] F. Pollmann, A. M. Turner, E. Berg, and M. Oshikawa, Entanglement spectrum of a topological phase in one dimension, *Phys. Rev. B* **81**, 064439 (2010).
- [8] F. Pollmann, E. Berg, A. M. Turner, and M. Oshikawa, Symmetry protection of topological phases in one-dimensional quantum spin systems, *Phys. Rev. B* **85**, 075125 (2012).
- [9] A. Meyer, A. Gleizes, J. J. Girerd, M. Verdaguer, and O. Kahn, Crystal structures, magnetic anisotropy properties and orbital interactions in catena-(mu.-nitrito)-bis(ethylenediamine)nickel(II) perchlorate and triiodide, *Inorg. Chem.* **21**, 1729 (1982).
- [10] J. P. Renard, M. Verdaguer, L. P. Regnault, W. A. C. Erkelens, J. Rossat-Mignod, and W. G. Stirling, Presumption for a quantum energy gap in the quasi-one-dimensional $S = 1$ Heisenberg antiferromagnet $\text{Ni}(\text{C}_2\text{H}_8\text{N}_2)_2\text{NO}_2(\text{ClO}_4)$, *Europhys. Lett.* **3**, 945 (1987).
- [11] S. Ma, C. Broholm, D. H. Reich, B. J. Sternlieb, and R. W. Erwin, Dominance of long-lived excitations in the antiferromagnetic spin-1 chain NENP, *Phys. Rev. Lett.* **69**, 3571 (1992).
- [12] D. Buttrey, J. Sullivan, and A. Rheingold, Phase equilibrium study of the Y-Ba-Ni-O system and structural characterization of the new quasi-one-dimensional oxide Y_2BaNiO_5 , *J. Solid State Chem.* **88**, 291 (1990).
- [13] J. Darriet and L. Regnault, The compound Y_2BaNiO_5 : A new example of a haldane gap in a $S = 1$ magnetic chain, *Solid State Commun.* **86**, 409 (1993).
- [14] G. Xu, J. F. DiTusa, T. Ito, K. Oka, H. Takagi, C. Broholm, and G. Aeppli, Y_2BaNiO_5 : A nearly ideal realization of the $S = 1$ Heisenberg chain with antiferromagnetic interactions, *Phys. Rev. B* **54**, R6827 (1996).
- [15] A. Nag, A. Nocera, S. Agrestini, M. Garcia-Fernandez, A. C. Walters, S.-W. Cheong, S. Johnston, and K.-J. Zhou, Quadrupolar magnetic excitations in an isotropic spin-1 antiferromagnet, *Nat. Commun.* **13**, 2327 (2022).
- [16] H. Mutka, C. Payen, P. Molinié, J. L. Soubeyrou, P. Colombet, and A. D. Taylor, Dynamic structure factor $[S(Q, \omega)]$ of the $S = 1$ quasi-one-dimensional Heisenberg antiferromagnet: Neutron-scattering study on AgVP_2S_6 , *Phys. Rev. Lett.* **67**, 497 (1991).
- [17] T. Asano, Y. Ajiro, M. Mekata, H. Yamazaki, N. Hosoi, T. Shinjo, and H. Kikuchi, Single crystal susceptibility of the $S = 1$ one-dimensional Heisenberg antiferromagnet AgVP_2S_6 , *Solid State Commun.* **90**, 125 (1994).
- [18] V. Gadet, M. Verdaguer, V. Briois, A. Gleizes, J. P. Renard, P. Beauvillain, C. Chappert, T. Goto, K. Le Dang, and P. Veillet, Structural and magnetic properties of $(\text{CH}_3)_4\text{NNi}(\text{NO}_2)_3$: A Haldane-gap system, *Phys. Rev. B* **44**, 705 (1991).
- [19] W. J. L. Buyers, R. M. Morra, R. L. Armstrong, M. J. Hogan, P. Gerlach, and K. Hirakawa, Experimental evidence for the Haldane gap in a spin-1 nearly isotropic, antiferromagnetic chain, *Phys. Rev. Lett.* **56**, 371 (1986).
- [20] E. Clar and D. G. Stewart, Aromatic hydrocarbons. LXV. Triangulene derivatives, *J. Am. Chem. Soc.* **75**, 2667 (1953).
- [21] N. Pavliček, A. Mistry, Z. Majzik, N. Moll, G. Meyer, D. J. Fox, and L. Gross, Synthesis and characterization of triangulene, *Nat. Nanotechnol.* **12**, 308 (2017).
- [22] S. Mishra, G. Catarina, F. Wu, R. Ortiz, D. Jacob, K. Eimre, J. Ma, C. A. Pignedoli, X. Feng, P. Ruffieux, J. Fernández-Rossier, and R. Fasel, Observation of fractional edge excitations in nanographene spin chains, *Nature (London)* **598**, 287 (2021).
- [23] J. Hieulle, S. Castro, N. Friedrich, A. Vegliante, F. R. Lara, S. Sanz, D. Rey, M. Corso, T. Frederiksen, J. I. Pascual, and D. Peña, On-surface synthesis and collective spin excitations of a triangulene-based nanostar, *Angew. Chem., Int. Ed.* **60**, 25224 (2021).
- [24] A. Delgado, C. Dusold, J. Jiang, A. Cronin, S. G. Louie, and F. R. Fischer, Evidence for excitonic insulator ground state in triangulene Kagome lattice, *arXiv:2301.06171*.
- [25] T. Kennedy, E. H. Lieb, and H. Tasaki, A two-dimensional isotropic quantum antiferromagnet with unique disordered ground state, *J. Stat. Phys.* **53**, 383 (1988).
- [26] F. Verstraete and J. I. Cirac, Valence-bond states for quantum computation, *Phys. Rev. A* **70**, 060302(R) (2004).
- [27] A. Miyake, Quantum computational capability of a 2D valence bond solid phase, *Ann. Phys.* **326**, 1656 (2011).
- [28] T.-C. Wei, I. Affleck, and R. Raussendorf, Affleck-Kennedy-Lieb-Tasaki state on a honeycomb lattice is a universal quantum computational resource, *Phys. Rev. Lett.* **106**, 070501 (2011).

- [29] T.-C. Wei, P. Haghnegahdar, and R. Raussendorf, Hybrid valence-bond states for universal quantum computation, *Phys. Rev. A* **90**, 042333 (2014).
- [30] R. Ganesh, D. N. Sheng, Y.-J. Kim, and A. Paramekanti, Quantum paramagnetic ground states on the honeycomb lattice and field-induced Néel order, *Phys. Rev. B* **83**, 144414 (2011).
- [31] A. Garcia-Saez, V. Murg, and T.-C. Wei, Spectral gaps of Affleck-Kennedy-Lieb-Tasaki Hamiltonians using tensor network methods, *Phys. Rev. B* **88**, 245118 (2013).
- [32] C.-Y. Huang, X. Chen, and F.-L. Lin, Symmetry-protected quantum state renormalization, *Phys. Rev. B* **88**, 205124 (2013).
- [33] K. Wierschem and K. S. D. Beach, Detection of symmetry-protected topological order in AKLT states by exact evaluation of the strange correlator, *Phys. Rev. B* **93**, 245141 (2016).
- [34] N. Pomata and T.-C. Wei, Demonstrating the Affleck-Kennedy-Lieb-Tasaki spectral gap on 2D degree-3 lattices, *Phys. Rev. Lett.* **124**, 177203 (2020).
- [35] M. Lemm, A. W. Sandvik, and L. Wang, existence of a spectral Gap in the Affleck-Kennedy-Lieb-Tasaki model on the hexagonal lattice, *Phys. Rev. Lett.* **124**, 177204 (2020).
- [36] J. I. Cirac, D. Poilblanc, N. Schuch, and F. Verstraete, Entanglement spectrum and boundary theories with projected entangled-pair states, *Phys. Rev. B* **83**, 245134 (2011).
- [37] B. Sriram Shastry and B. Sutherland, Exact ground state of a quantum mechanical antiferromagnet, *Physica B+C* **108**, 1069 (1981).
- [38] S. Miyahara and K. Ueda, Exact dimer ground state of the two dimensional Heisenberg spin system $\text{SrCu}_2(\text{BO}_3)_2$, *Phys. Rev. Lett.* **82**, 3701 (1999).
- [39] A. Koga and N. Kawakami, Quantum phase transitions in the Shastry-Sutherland model for $\text{SrCu}_2(\text{BO}_3)_2$, *Phys. Rev. Lett.* **84**, 4461 (2000).
- [40] B. Zhao, P. Weinberg, and A. W. Sandvik, Symmetry-enhanced discontinuous phase transition in a two-dimensional quantum magnet, *Nat. Phys.* **15**, 678 (2019).
- [41] J. Y. Lee, Y.-Z. You, S. Sachdev, and A. Vishwanath, Signatures of a deconfined phase transition on the Shastry-Sutherland lattice: Applications to quantum critical $\text{SrCu}_2(\text{BO}_3)_2$, *Phys. Rev. X* **9**, 041037 (2019).
- [42] J. Yang, A. W. Sandvik, and L. Wang, Quantum criticality and spin liquid phase in the Shastry-Sutherland model, *Phys. Rev. B* **105**, L060409 (2022).
- [43] L. Wang, Y. Zhang, and A. W. Sandvik, Quantum spin liquid phase in the Shastry-Sutherland model detected by an improved level spectroscopic method, *Chin. Phys. Lett.* **39**, 077502 (2022).
- [44] H. Kageyama, K. Yoshimura, R. Stern, N. V. Mushnikov, K. Onizuka, M. Kato, K. Kosuge, C. P. Slichter, T. Goto, and Y. Ueda, Exact dimer ground state and quantized magnetization plateaus in the two-dimensional spin system $\text{SrCu}_2(\text{BO}_3)_2$, *Phys. Rev. Lett.* **82**, 3168 (1999).
- [45] S. Haravifard, D. Graf, A. E. Feiguin, C. D. Batista, J. C. Lang, D. M. Silevitch, G. Srajer, B. D. Gaulin, H. A. Dabkowska, and T. F. Rosenbaum, Crystallization of spin superlattices with pressure and field in the layered magnet $\text{SrCu}_2(\text{BO}_3)_2$, *Nat. Commun.* **7**, 11956 (2016).
- [46] M. E. Zayed, C. Rüegg, J. Larrea J., A. M. Läuchli, C. Panagopoulos, S. S. Saxena, M. Ellerby, D. F. McMorrow, T. Strässle, S. Klotz, G. Hamel, R. A. Sadykov, V. Pomjakushin, M. Boehm, M. Jiménez-Ruiz, A. Schneidewind, E. Pomjakushina, M. Stingaciu, K. Conder, and H. M. Rønnow, 4-spin plaquette singlet state in the Shastry-Sutherland compound $\text{SrCu}_2(\text{BO}_3)_2$, *Nat. Phys.* **13**, 962 (2017).
- [47] J. Guo, G. Sun, B. Zhao, L. Wang, W. Hong, V. A. Sidorov, N. Ma, Q. Wu, S. Li, Z. Y. Meng, A. W. Sandvik, and L. Sun, Quantum phases of $\text{SrCu}_2(\text{BO}_3)_2$ from high-pressure thermodynamics, *Phys. Rev. Lett.* **124**, 206602 (2020).
- [48] J. L. Jiménez, S. P. G. Crone, E. Fogh, M. E. Zayed, R. Lortz, E. Pomjakushina, K. Conder, A. M. Läuchli, L. Weber, S. Wessel, A. Honecker, B. Normand, C. Rüegg, P. Corboz, H. M. Rønnow, and F. Mila, A quantum magnetic analogue to the critical point of water, *Nature (London)* **592**, 370 (2021).
- [49] Y. Cui, L. Liu, H. Lin, K.-H. Wu, W. Hong, X. Liu, C. Li, Z. Hu, N. Xi, S. Li, R. Yu, A. W. Sandvik, and W. Yu, Proximate deconfined quantum critical point in $\text{SrCu}_2(\text{BO}_3)_2$, *Science* **380**, 1179 (2023).
- [50] H. Kageyama, Y. Ueda, Y. Narumi, K. Kindo, M. Kosaka, and Y. Uwatoko, Crossbreeding between experiment and theory on orthogonal dimer spin system, *Prog. Theor. Phys. Suppl.* **145**, 17 (2002).
- [51] M. Taibi, J. Aride, J. Darriet, A. Moqine, and A. Boukhari, Structure cristalline de l'oxyde $\text{Nd}_2\text{BaZnO}_5$, *J. Solid State Chem.* **86**, 233 (1990).
- [52] K. Siemensmeyer, E. Wulf, H.-J. Mikeska, K. Flachbart, S. Gabáni, S. Mat'áš, P. Priputen, A. Efdokimova, and N. Shitsevalova, Fractional magnetization plateaus and magnetic order in the Shastry-Sutherland magnet TmB_4 , *Phys. Rev. Lett.* **101**, 177201 (2008).
- [53] M. Marshall, B. R. Billingsley, X. Bai, Q. Ma, T. Kong, and H. Cao, Field-induced partial disorder in a Shastry-Sutherland lattice, *Nat. Commun.* **14**, 3641 (2023).
- [54] A. Koga and N. Kawakami, Frustration-induced phase transitions in the spin- S orthogonal-dimer chain, *Phys. Rev. B* **65**, 214415 (2002).
- [55] A. Koga and N. Kawakami, Quantum phase transitions in a frustrated orthogonal-dimer $S = 1$ spin system, *Phys. B: Condens. Matter* **329-333**, 1267 (2003).
- [56] A. Koga, N. Kawakami, and M. Sigrist, Quantum phase transitions of the $S = 1$ Shastry-Sutherland model, *J. Phys. Soc. Jpn.* **72**, 938 (2003).
- [57] P. Fazekas, *Lecture Notes on Electron Correlation and Magnetism* (World Scientific, Singapore, 1999).
- [58] S.-S. Gong, W. Zhu, D. N. Sheng, and K. Yang, Possible nematic spin liquid in spin-1 antiferromagnetic system on the square lattice: Implications for the nematic paramagnetic state of FeSe, *Phys. Rev. B* **95**, 205132 (2017).
- [59] C. Lacroix, P. Mendels, and F. Mila, *Introduction to Frustrated Magnetism: Materials, Experiments, Theory* (Springer, New York, 2011).
- [60] C. Kittel, Model of exchange-inversion magnetization, *Phys. Rev.* **120**, 335 (1960).
- [61] M. Fishman, S. R. White, and E. M. Stoudenmire, The ITensor Software Library for Tensor Network Calculations, *SciPost Phys. Codebases* **4** (2022).
- [62] M. Blume and Y. Y. Hsieh, Biquadratic exchange and quadrupolar ordering, *J. Appl. Phys.* **40**, 1249 (1969).
- [63] A. Läuchli, F. Mila, and K. Penc, Quadrupolar phases of the $S = 1$ bilinear-biquadratic Heisenberg model on the triangular lattice, *Phys. Rev. Lett.* **97**, 087205 (2006).

- [64] H. Li and F. D. M. Haldane, Entanglement spectrum as a generalization of entanglement entropy: Identification of topological order in non-Abelian fractional quantum hall effect states, *Phys. Rev. Lett.* **101**, 010504 (2008).
- [65] X.-L. Qi, H. Katsura, and A. W. W. Ludwig, General relationship between the entanglement spectrum and the edge state spectrum of topological quantum states, *Phys. Rev. Lett.* **108**, 196402 (2012).
- [66] G. Moore and N. Seiberg, Classical and quantum conformal field theory, *Commun. Math. Phys.* **123**, 177 (1989).
- [67] P. Calabrese and J. Cardy, Entanglement entropy and quantum field theory, *J. Stat. Mech.* (2004) P06002.
- [68] K. Hallberg, X. Q. G. Wang, P. Horsch, and A. Moreo, Critical behavior of the $S = 3/2$ antiferromagnetic Heisenberg chain, *Phys. Rev. Lett.* **76**, 4955 (1996).
- [69] F. Michaud, S. R. Manmana, and F. Mila, Realization of higher Wess-Zumino-Witten models in spin chains, *Phys. Rev. B* **87**, 140404(R) (2013).
- [70] N. Chepiga, I. Affleck, and F. Mila, Floating, critical, and dimerized phases in a frustrated spin- $\frac{3}{2}$ chain, *Phys. Rev. B* **101**, 174407 (2020).
- [71] J. K. Glasbrenner, I. I. Mazin, H. O. Jeschke, P. J. Hirschfeld, R. M. Fernandes, and R. Valentí, Effect of magnetic frustration on nematicity and superconductivity in iron chalcogenides, *Nat. Phys.* **11**, 953 (2015).
- [72] A. Kartsev, M. Augustin, R. F. L. Evans, K. S. Novoselov, and E. J. G. Santos, Biquadratic exchange interactions in two-dimensional magnets, *npj Comput. Mater.* **6**, 150 (2020).
- [73] U. Schollwöck, T. Jolicoeur, and T. Garel, Onset of incommensurability at the valence-bond-solid point in the $S = 1$ quantum spin chain, *Phys. Rev. B* **53**, 3304 (1996).
- [74] G. Fáth and J. Sólyom, Period tripling in the bilinear-biquadratic antiferromagnetic $S = 1$ chain, *Phys. Rev. B* **44**, 11836 (1991).
- [75] A. Läuchli, G. Schmid, and S. Trebst, Spin nematics correlations in bilinear-biquadratic $S = 1$ spin chains, *Phys. Rev. B* **74**, 144426 (2006).
- [76] C. Itoi and M.-H. Kato, Extended massless phase and the Haldane phase in a spin-1 isotropic antiferromagnetic chain, *Phys. Rev. B* **55**, 8295 (1997).
- [77] S. Chen, L. Wang, Y. Hao, and Y. Wang, Intrinsic relation between ground-state fidelity and the characterization of a quantum phase transition, *Phys. Rev. A* **77**, 032111 (2008).
- [78] H. Suwa, A. Sen, and A. W. Sandvik, Level spectroscopy in a two-dimensional quantum magnet: Linearly dispersing spinons at the deconfined quantum critical point, *Phys. Rev. B* **94**, 144416 (2016).
- [79] L. Wang and A. W. Sandvik, Critical level crossings and gapless spin liquid in the square-lattice spin- $1/2 J_1 - J_2$ Heisenberg antiferromagnet, *Phys. Rev. Lett.* **121**, 107202 (2018).
- [80] Y. Nomura and M. Imada, Dirac-type nodal spin liquid revealed by refined quantum many-body solver using neural-network wave function, correlation ratio, and level spectroscopy, *Phys. Rev. X* **11**, 031034 (2021).
- [81] T. Sakai and M. Takahashi, The ground state of quasi-one-dimensional Heisenberg antiferromagnets, *J. Phys. Soc. Jpn.* **58**, 3131 (1989).
- [82] A. Koga and N. Kawakami, Quantum phase transitions for the Haldane system in higher dimensions: A mixed-spin cluster expansion approach, *Phys. Rev. B* **61**, 6133 (2000).
- [83] Y. J. Kim and R. J. Birgeneau, Monte Carlo study of the $S = \frac{1}{2}$ and $S = 1$ Heisenberg antiferromagnet on a spatially anisotropic square lattice, *Phys. Rev. B* **62**, 6378 (2000).
- [84] M. Matsumoto, C. Yasuda, S. Todo, and H. Takayama, Ground-state phase diagram of quantum Heisenberg antiferromagnets on the anisotropic dimerized square lattice, *Phys. Rev. B* **65**, 014407 (2001).
- [85] K. Wierschem and P. Sengupta, Quenching the Haldane gap in spin-1 Heisenberg antiferromagnets, *Phys. Rev. Lett.* **112**, 247203 (2014).
- [86] I. Niesen and P. Corboz, Emergent Haldane phase in the $S = 1$ bilinear-biquadratic Heisenberg model on the square lattice, *Phys. Rev. B* **95**, 180404(R) (2017).
- [87] W.-J. Hu, S.-S. Gong, H.-H. Lai, H. Hu, Q. Si, and A. H. Nevidomskyy, Nematic spin liquid phase in a frustrated spin-1 system on the square lattice, *Phys. Rev. B* **100**, 165142 (2019).
- [88] J.-Y. Chen, S. Capponi, and D. Poilblanc, Discrete lattice symmetry breaking in a two-dimensional frustrated spin-1 Heisenberg model, *Phys. Rev. B* **98**, 045106 (2018).
- [89] W.-J. Hu, S.-S. Gong, H.-H. Lai, Q. Si, and E. Dagotto, Density matrix renormalization group study of nematicity in two dimensions: Application to a spin-1 bilinear-biquadratic model on the square lattice, *Phys. Rev. B* **101**, 014421 (2020).
- [90] X.-T. Zhang, W.-J. Hu, E. Dagotto, and S. Gong, Fragility of the nematic spin liquid induced by diagonal couplings in the square-lattice SU(3) model, *Phys. Rev. B* **104**, 195135 (2021).